

Journal of Materials Chemistry A

Materials for energy and sustainability

Accepted Manuscript

This article can be cited before page numbers have been issued, to do this please use: M. Ambrico, O. Durante, S. De Stefano, R. D'Orsi, D. Aceto, P. F. Ambrico, N. Martucciello, F. Giubileo, S. RIVAS, A. Operamolla and A. Di Bartolomeo, *J. Mater. Chem. A*, 2025, DOI: 10.1039/D5TA05024C.



This is an Accepted Manuscript, which has been through the Royal Society of Chemistry peer review process and has been accepted for publication.

Accepted Manuscripts are published online shortly after acceptance, before technical editing, formatting and proof reading. Using this free service, authors can make their results available to the community, in citable form, before we publish the edited article. We will replace this Accepted Manuscript with the edited and formatted Advance Article as soon as it is available.

You can find more information about Accepted Manuscripts in the [Information for Authors](#).

Please note that technical editing may introduce minor changes to the text and/or graphics, which may alter content. The journal's standard [Terms & Conditions](#) and the [Ethical guidelines](#) still apply. In no event shall the Royal Society of Chemistry be held responsible for any errors or omissions in this Accepted Manuscript or any consequences arising from the use of any information it contains.

Lignin for sustainable electronics: Interplay of structure, morphology and chemistry in modelling dielectric properties

Marianna Ambrico¹, Ofelia Durante^{2,}, Sebastiano De Stefano², Rosarita D'Orsi³, Domenico Aceto¹, Paolo Francesco Ambrico¹, Nadia Martucciello⁴, Filippo Giubileo⁴, Sandra Rivas⁵, Alessandra Operamolla^{3,*}, and Antonio Di Bartolomeo²*

*Corresponding authors: odurante@unisa.it, alessandra.operamolla@unipi.it

¹ CNR – ISTP, Institute for Plasma Science and Technology, Via Giovanni Amendola 122/d, Bari 70126, Italy

² Department of Physics “E.R. Caianiello”, University of Salerno, Via Giovanni Paolo II 132, Fisciano (Sa) 84084, Italy

³ Department of Chemistry and Industrial Chemistry, University of Pisa, Via Giuseppe Moruzzi 13, Pisa 56124, Italy

⁴ CNR-SPIN, Salerno Unit, Via Giovanni Paolo II 132, Fisciano (Sa) 84084, Italy

⁵ Department of Chemical Engineering, Faculty of Science of Ourense, University of Vigo, As Lagoas s/n 32004 Ourense, Spain



Abstract

View Article Online
DOI: 10.1039/D5TA05024C

The search for promising and sustainable materials for advanced electronic applications has recently drawn attention to lignin. As a major by-product of pulping processes, lignin features a complex aromatic structure rich in aliphatic and aromatic ethers, as well as hydroxyl and carboxyl functional groups, which endow it with unique chemical and electronic properties. In this study, we present a comparative analysis of three distinct lignins. Two of them (L1 and L2) are derived from the Kraft pulping process, while the third (L3) is extracted from *Cynara cardunculus* using an ethanolic *organosolv* method. These lignins are investigated as active layers in an interdigitated electronic device. To explore in depth the influence of the compositional, structural, morphological and chemical properties of the three lignins on dielectric relaxation dynamics and charge transport mechanisms, several advanced analytical techniques were adopted, including Electrical Impedance Spectroscopy (EIS), Nyquist Plots (NP), Broadband Dielectric Spectroscopy (BDS), and Complex Power (CP) representations. Our consistent workflow included the same interdigitated electrodes (IDE) platform, identical frequency window, a unified BDS formalism, and a common base EIS circuit design tailored to the observed Nyquist Plot features. Our findings revealed that the extraction process enables tuning of the lignins properties. Whilst L1 exhibits smooth, compact morphology and a higher polymerization degree, limiting charge mobility and resulting in inferior electrical and capacitive performance, L2 features a fibrous structure with higher content in carboxyl groups and ashes, which significantly enhances conductivity and capacitance. L3 displays an intermediate morphology with a high concentration of aliphatic hydroxyl groups, offering a balanced blend of chemical and structural properties. Furthermore, we reveal the potential of lignin as a versatile dielectric material exhibiting super capacitive behavior among other properties.

Keywords *lignin; organosolv lignin; lignin-based devices; AC charge transport; Impedance and Dielectric spectroscopy; supercapacitor*

1. Introduction

Lignin accounts for approximately 20–30% of the dry weight of lignocellulosic biomass,¹ and constitutes a renewable resource for a variety of cutting-edge applications. The unique physicochemical properties of lignin, such as its thermal stability and redox activity, make it an attractive candidate in different fields^{2,3}. However, the structural complexity of lignin offers both opportunities and challenges for its utilization. Lignin's high content of aromatic and phenol groups imparts strong antioxidant and redox properties, which are essential for energy storage devices such as supercapacitors and batteries^{4–6}. Studies have demonstrated that incorporating lignin into



electrodes not only improves their electrochemical performance but also reduces production costs and environmental impact, aligning with the principles of green chemistry⁷⁻⁹. Moreover, lignin-derived activated carbons, carbon nanofibers, and mesoporous carbons, have emerged as leading candidates for electrode materials¹⁰. Furthermore, lignin has garnered attention for its intrinsic dielectric and capacitive properties^{11,12}. As an amorphous polymer with a complex network of aromatic rings and ether linkages, lignin exhibits dielectric behavior suitable for use in memory devices. For example, lignin-based resistive switching random access memory (RRAM) devices have shown promise for high-density information storage, leveraging lignin's ability to form multilevel resistance states^{13,14}. Recent studies have also demonstrated the potential of lignin as a gate dielectric material in organic field-effect transistors (OFETs)^{7,15}. Specifically, Kraft lignin has shown promising results as a dielectric layer in bottom-gate OFETs, offering reliable electrical performance along with environmentally friendly characteristics⁷. On the other hand, lignin extracted through the *organosolv* process - known for its higher purity and better solubility in organic solvents - has yet to be explored for use in electronic devices. From a broader perspective, Kraft pulping and organosolv extraction represent contrasting technological and sustainability paradigms. Kraft pulping is primarily designed to delignify biomass or cellulose fiber recovery, producing lignin as a byproduct along with sulfur-containing residues, degraded carbohydrates and inorganic salts. These lignins are heterogeneous, partially condensed and contain residual inorganic compounds.¹⁶ In contrast, organosolv processes, use organic solvent under milder conditions, yielding higher-purity lignin with lower sulfur content, more defined hydroxyl functionality and improved solubility for high-value applications. From a sustainable perspective, Kraft pulping is cost-effective and scalable, but generates chemical effluents, whereas *organosolv* processes offer environmental advantages despite higher production costs. Then, the choice of extraction method fundamentally influences both, the structural and chemical characteristics of lignin, with in turn dictate its technological performance across diverse applications. **L1**, **L2** and **L3** were deliberately chosen to encompass a relevant technological spectrum. **L1** and **L2** are widely available from industrial pulping processes, while the biomass-derived *organosolv* **L3** introduces a higher-purity variant with enhanced functional accessibility.¹⁷

Many factors influence the electrical behavior of lignin, which are encountered only to a limited extent in synthetic organic polymers. Lignin is a random copolymer of *p*-coumaryl, coniferyl and sinapyl alcohols^{18,19}, for which there is limited knowledge about its chemical connectivity, especially in terms of the true sequence of the repeating units. This makes even theoretical predictions of lignin properties, in terms of self-aggregation, highly difficult. Furthermore, the extraction methods used for lignin isolation leave a fingerprint over the isolated material, which involves the presence of



impurities in the isolated product^{20,21} and molecular skeleton modification. Often, technical lignins contain ashes or residual proteins or sugars; nonetheless, many other studies apply lignin in electronic devices without correlating the performance with the eventual presence of impurities, which, in some cases, may not be negligible^{5,8,11,22}.

This study aims to be a follow up of previous study on three lignins : two of them (**L1** and **L2**) sourced from the Kraft pulping process and one (**L3**) derived from *Cynara cardunculus* using an *organosolv* extraction method.²³ All samples are solution-processed under identical conditions to ensure consistency. Due to their distinct chemical compositions and extraction methods, the three lignins exhibit varied ashes and functional groups content (phenolic and aliphatic OH, carboxyl groups, sulfur content etc.) and aggregation behaviors, which in turn influence their device performance, and are parametrized in this study to identify factors allowing to assess lignin pathways to valorization in electronic devices. In this context, the adoption of the Electrical Impedance Spectroscopy (EIS) and Broadband Dielectric Spectroscopy (BDS) has proven particularly suitable for providing insights into the correlation between the complex polymeric nature, morphology and chemistry of lignins with their charge carrier storage and transport properties. These insights are crucial for evaluating their potential applications in various electronic and energy storage devices. Unlike the DC current-voltage response, EIS and BDS rely on the response under an AC field which enables the capture of signals from polymeric chains oscillations, ionic charge current and distributions, as well as redox reactions signals^{24–29}. In summary, this study sheds light on the different properties of lignin that can be fine-tuned selecting the production process. We aim to offer new insights, positioning lignin as a versatile material for future dielectric and energy storage applications.

2. Results and discussion

2.1 AC electrical characterization

Solutions of the three lignins were prepared in EtOH:NH₄OH in volumetric ratio 1:1 at 20 mg mL⁻¹ concentration. The solutions were drop-cast onto circular Ti/Au interdigitated electrodes (IDEs) (MICRUX, $\phi = 3.5$ mm, 90 finger pairs, 90 μm width/gap) under ambient conditions (20 °C, 50% RH). More information on the morphological, chemical and structural properties of the materials are reported in **Table S1**, **Figures S1** and **S2** of the Supplementary Information, and in the ref.³⁰. Prior to deposition, the suspension was stirred for 5 minutes at 2000 rpm and the electrodes were ultrasonically cleaned in isopropyl alcohol and dried in air; all depositions were performed in triplicate to ensure reproducible impedance responses. Replicate depositions produced overlapping spectra and measured film thicknesses around 0.35–0.40 μm by atomic force microscopy (RMS roughness ~ 107 nm).¹³



2.1. Nyquist plots

Electrical impedance spectroscopy (EIS) uses the Nyquist plot (NP) representation of the impedance Z , where the x-axis represents the real part of the impedance ($\text{Re}Z$), indicative of the resistance of the system. The y-axis represents the imaginary part of the impedance ($-\text{Im} Z$) that is associated with the capacitive properties of the system. In an NP representation, the frequency decreases from the left to the right of the plot, and the behavior is represented via a specific combination of electrical circuit components³¹. More details on the features of the circuit elements adopted in this work and their response vs. the AC frequency are shown in the **Figure S3** of the Electronic Supplementary Information (ESI).

In **Figure 1**, we report the experimental (symbols) and best-fit (straight lines) NP spectra in the full frequency range (1.0 MHz–0.1 Hz from left to right) at 0.0 V and at ± 0.8 V for **L1 (Figure 1a)**, **L2 (Figure 1b)**, and **L3 (Figure 1c)** on IDE devices together with the equivalent circuits simulating the experimental data at both DC voltages (**Figures 1d,e**). The values of the circuit parameters extracted by the EIS analyzer software³² are summarized in the **Table S2** of Supplementary Information. The choice of applied DC polarization (0.0 V and ± 0.8 V) was made to exclude from the electrochemical window the redox potential of water, ensuring the assessment of the electrical symmetry of the device at positive and negative voltages. This allowed us to study the potential charge transfer processes and the possible occurrence of redox activity, with regard to ionic and electronic transport mechanisms.



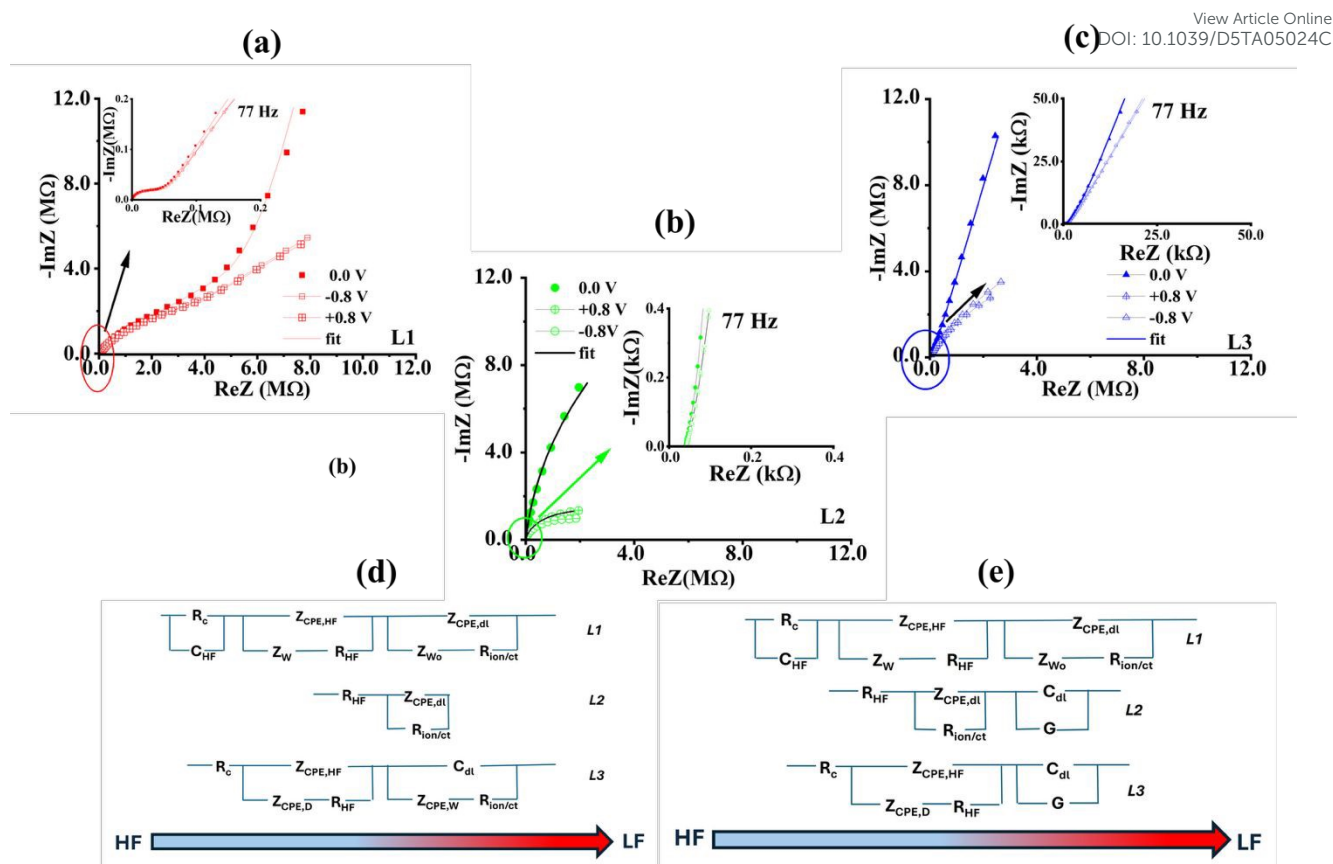


Figure 1. Impedance spectroscopy representation via Nyquist Plots for devices **L1** (a), **L2** (b) and **L3** (c) from 1 MHz to 0.1 Hz, at 0.0 V and with a bias of ± 0.8 V DC. The insets show the high and medium frequency range (1 MHz-77 Hz). The equivalent circuits (d, e) model the electrical behaviour at 0.0 V (d) and ± 0.8 V (e). The arrows indicate the active components at high (HF) and low frequencies (LF). In **L2** and **L3**, the Gerischer impedance (G) appears at ± 0.8 V, suggesting chemical reactions prior to the oxidation-reduction process³³. The electrical circuits simulating the NPs were built up by using the EIS analyzer software³⁴.

A preliminary insight into the full NP behavior at 0.0 V_{DC} revealed significant differences in the **L1** device with respect to the **L2** and **L3** devices, which were mainly visible in the low-frequency range (**Figure 1a-c**, right side of the plot). Moreover, **L2** exhibits a distinctive feature, with a low resistance at high frequency and the sharp onset of a dominant capacitive contribution toward lower frequency. The NP magnifications (**Figure 1a-c**, insets for high and medium frequencies, and **Figure S4** in the ESI) revealed other specific fingerprints vs. the frequency, not visible in the full spectra, and allowed to capture differences and similarities in the AC response among the three lignin devices.

At higher frequencies, the **L1** (**Figure 1a** inset and **Figure S4**) and **L3** (**Figure 1c** inset) show comparable electrical behavior, whereas **L2**'s response (**Figure 1b**) is essentially dominated by a small resistance and, again, by the onset of capacitive behavior. Furthermore, this is characterized by a sharp increase in ImZ, yielding a curve almost parallel to the y-axis, a trend generally observed in supercapacitors³⁵. Notably, the module of the experimental impedance $|Z|$ and, more specifically, the



values at high frequency of the real part $\text{Re}Z$ due to the only resistive response, passes from $20 \text{ k}\Omega$ in **L1** to 887Ω in **L3** and 46Ω in **L2** (see **Figure S4** in the Supplementary Information), justifying the DC currents observed in the I-V characterizations³⁰.

Following the experimental evidence, **L1** and **L3** can be modeled by similar equivalent circuit structures, whereas a different model is required for **L2**. Notably, similar behavior is present at both positive $V_{\text{DC}} = +0.8 \text{ V}$ and negative $V_{\text{DC}} = -0.8 \text{ V}$ because of the almost ohmic behavior of the Au IDE contacts. Therefore, we focus our attention on the cases in which $V_{\text{DC}} = 0.0 \text{ V}$ and $V_{\text{DC}} = +0.8 \text{ V}$. In this approach, the NP behavior (either $0.0 \text{ V}_{\text{DC}}$ or $V_{\text{DC}} = \pm 0.8 \text{ V}$) can be described in two main sections: the *first* extends in the frequency range of 1.0 MHz – 77 Hz (high–mid-frequency region), and the *second* extends from 77 Hz – 0.1 Hz (mid–low-frequency region). Details on the development of the various regions of the spectra represented per frequency decade and justifying the modeling are reported in **Figure S4** of the Supplementary Information.

At $V_{\text{DC}} = 0.0 \text{ V}$, modeling of the NPs was performed using the free downloadable EIS analyzer software³⁶ and the equivalent electrical circuits shown in **Figure 1d** for the **L1**, **L2** and **L3**, respectively. The components are arranged in order of frequency, starting from the high-frequency (HF) region on the left and progressing to the low-frequency (LF) region on the right. The equivalent circuits applicable at $V_{\text{DC}} = \pm 0.8 \text{ V}$ are summarized in **Figure 1e**.

For **L1** (**Figure 1a**) and **L3** (**Figure 1c**), the equivalent circuit consists of *two sections* made up of Randle-like circuits (**Figure 1d**, the sections marked by the arrow colored from blue (HF) to red (LF))²⁸, one effective in the high–mid-frequency range and the other in the low-frequency range. Compared with the AC conductivity spectra (see next section), the first section of the circuit, covering four decades, was assigned to ionic diffusion, electrode polarization and ionic hopping, whereas the second was assigned to the lignin redox features.

In the *first section*, the lower branch of the Randle's circuit is associated with free ionic charge diffusion and represented by a Warburg impedance (Z_{W}) in **L1** and a constant phase element $Z_{\text{CPE,D}}$ in **L3**. Notably, the impedance values (see **Table S1**, where $Z_{\text{CPE,D}} < Z_{\text{W}}$) and \mathbf{R}_{HF} in **L3** are lower than those in **L1**, suggesting that ionic charge diffusion is less hindered in **L3** compared to **L1**. A further element was added to represent the contact impedance ($\mathbf{R}_{\text{c}}//\mathbf{C}_{\text{HF}}$ in **L1**) or resistance (\mathbf{C}_{HF} in **L3**) at the lignin/Au_{IDE} interface. In the upper branch associated to the double layer, the corresponding impedance $Z_{\text{CPE,HF}}$ is much greater in **L3** than in **L1**, an effect that appears in the former as a sharp increase along the $-\text{Im}Z$ axis similarly to what observed in **L2**.



The *second section* (low frequency, LF) represents the transport at the 'Au_{IDE} (electrode)/lignin (electrolyte)' interface. The lower branch, labeled as faradaic, again includes Randle's-like circuits features i.e. the series of the $R_{ion/ct}$ with a Warburg open (Z_{W_o}) impedance in **L1** and with a constant phase element Z_{CPE1} in **L3**. In **L1** the adoption in the equivalent circuit of a Warburg open (Z_{W_o}) rather than a semi-infinite Warburg impedance Z_W ,^{35,37} is justified by the presence in the NP of a straight line with a slope greater than 45° (see EIS in the Supplementary Information). Overall, the series of the $R_{ion/ct}$ with the diffusion elements enable to estimate the magnitude of the charge transfer via redox reactions^{36,38} then the reactivity to the environment. Finally, in the upper branch the constant phase element Z_{CPEdl} in **L1** and a capacitor C_{dl} term in **L3** are placed parallel to the faradaic one and represent the charge double layer forming at the electrode/lignin interface.

L2 (Figure 1b) behavior stands out from **L1** and **L3**: here, the *first section* representing the NP consisted of a resistor named R_{HF} , corresponding to the intercept on the ReZ. The *second section* consists of the parallel of the double layer nonideal capacitance $Z_{CPE,dl}$ and of the ionic charge resistance $R_{ion/ct}$, as representative of the dominant extension of the impedance along the -ImZ. Moreover, $R_{ion/ct}$ is an index of the ability of the ionic charge to promote charge transfer (via redox reactions) at the electrodes. Notably, this circuit is typically encountered when simulating the NP of supercapacitor devices³⁵.

Finally, we found that the Z_{CPEdl} in **L3** places in between those of **L1** and **L2** (see **Table S2** in Supporting Information) and the high-frequency resistance decreases in the order $R_{HF}(L1) > R_{HF}(L3) > R_{HF}(L2)$ (see **Table S2** in the Supplementary Information), in agreement with the magnitude of the measured DC currents. Similarly, this sequence can be explained because of the features of the morphological structure shown in **Figure S1**.

In all the three lignin devices, the superposition of a DC bias (either positive or negative) to the AC one modified their response at low frequencies, although the extent of the response varied significantly. These changes can result, for example, from redox reactions at the electrode/lignin interface, producing charge transfer currents whose magnitude is represented by the resulting values of the charge transfer resistance $R_{ion/ct}$ under bias.

Again, in this range, **L2** and **L3** demonstrated a DC vehiculated response represented by the presence in **L2** either of a lower $R_{ct/ion}$ ($R_{ct/ion} = 3.5 \times 10^7 \Omega$ at 0.0 V and $R_{ct/ion} = 1.2 \times 10^6 \Omega$ at 0.8 V, see **Table S2** in Supporting Information) or a Gerisher impedance³³ and in **L3** of a solely Gerisher impedance. Therefore, these results further confirm the higher reactivity of both lignins due to the presence of adsorbates, as also suggested by the I-V measurement under different pressures³⁰. The



latter is furthermore indicative of mixed, albeit not distinguishable, electronic–ionic conduction due to a peculiar charge exchange current at the electrode/lignin interface, which is consistent with the occurrence of diffusion coupled with chemical reactions³³. Conversely, in the low-frequency section, when a bias is applied, the **L1** device retains the same behavior, as expressed by the similar order of magnitude of the values of $R_{ion/ct}$ in Randle's circuit and hints at lower or null reactivity, which is accompanied by a localized ionic charge diffusion mechanism expressed again by the Z_{W0} impedance element.

To summarize, at 0.0 V, **L1** and **L2** display peculiar circuits, the former being a superposition of HF and LF transport ascribed to ionic charge-free diffusion and redox properties at the lignin interface; conversely, **L2** displays a sharp and fast transition from a low impedance (resistive state) to a quasi-ideal capacitive state covering the full frequency. The circuit of lignin **L3** is similar to that of **L1** at high frequencies, whereas, at low frequencies, the electrical properties of **L3** are dominated by capacitive effects. The behavior can be interpreted in strict relation to morphology. The similarities of **L2** and **L3** increase at 0.8 V, indicating their interaction with the external environment. Indeed, the presence of a Gerisher impedance hints at more reactivity toward ambient gases.

2.2 Broadband dielectric spectroscopy (BDS) results

The BDSs is recognized as a powerful data representation for accessing impedance properties in polymeric materials,^{39–42} highlighting the molecular dynamics of materials in response to an AC field. In this framework, BDS allows to investigate in great detail the dielectric relaxation processes and AC charge transport at various time scales.^{25,43} Details on the mathematical formalism used in this section are provided in the Electronic Supplementary Information.

We found that the lignin polymer structure, morphology and chemistry strongly affect the permittivity $\varepsilon(\omega)$ (eq. S8) and AC conductivity $\sigma(\omega)$ (eq. S12) frequency dispersion features. The $D_{ln \omega} \varepsilon'(\omega)$ Kramers-Kronig representation of the permittivity $\varepsilon'(\omega)$ (eq. S10) is more suitable to enhance the elicited features via the presence of more resolved peaks at frequencies typical of specific lignin relaxation mechanisms.^{41,44} As a result, in **L1** (panel 2a, red curve), the first peak is due to β -relaxation and can be associated to the hydration status of the polymer⁴⁵ or to the radial charge hopping mechanism^{13,24}; the second peak is due to electrode polarization (EP). An additional relaxation process is observed and attributed to near-constant loss (NCL)⁴². Unlike **L1**, the $D_{ln \omega} \varepsilon'(\omega)$ of **L2** (panel 2a, green curve) exhibits a dominant relaxation process, hinting an extended EP, and a rise toward lower frequencies. However, in our previous findings, the measurements conducted on **L2** down to 1.0 mHz¹³ revealed the presence of two more peaks. The first one is termed as α -



relaxation and commonly associated to the polymeric chain length, i.e. the longer the chain, the lower the oscillation frequency⁴⁵; moreover, it can be qualitatively associated to the polymerization degree and/or to polymer aggregates dimension^{24,25}. The second peak is again representative of the elicited β -relaxation. Like **L1**, **L3** (panel 2a, blue curve) displays two distinct peaks in $D_{\text{In}}\omega\varepsilon'(\omega)$, corresponding to β -relaxation and EP, the latter extending less in frequency than in **L2**.⁴⁶ Additionally, in **L3**, α relaxation occurs at frequencies slightly higher than **L2**, which implies a lower extension of the polymer aggregates⁴⁷. The observed frequency location of the α -relaxation confirms what already discussed in our previous paper, i.e. due to the extraction process, the degree of polymerization scales down going from **L1** to **L2** and **L3**.

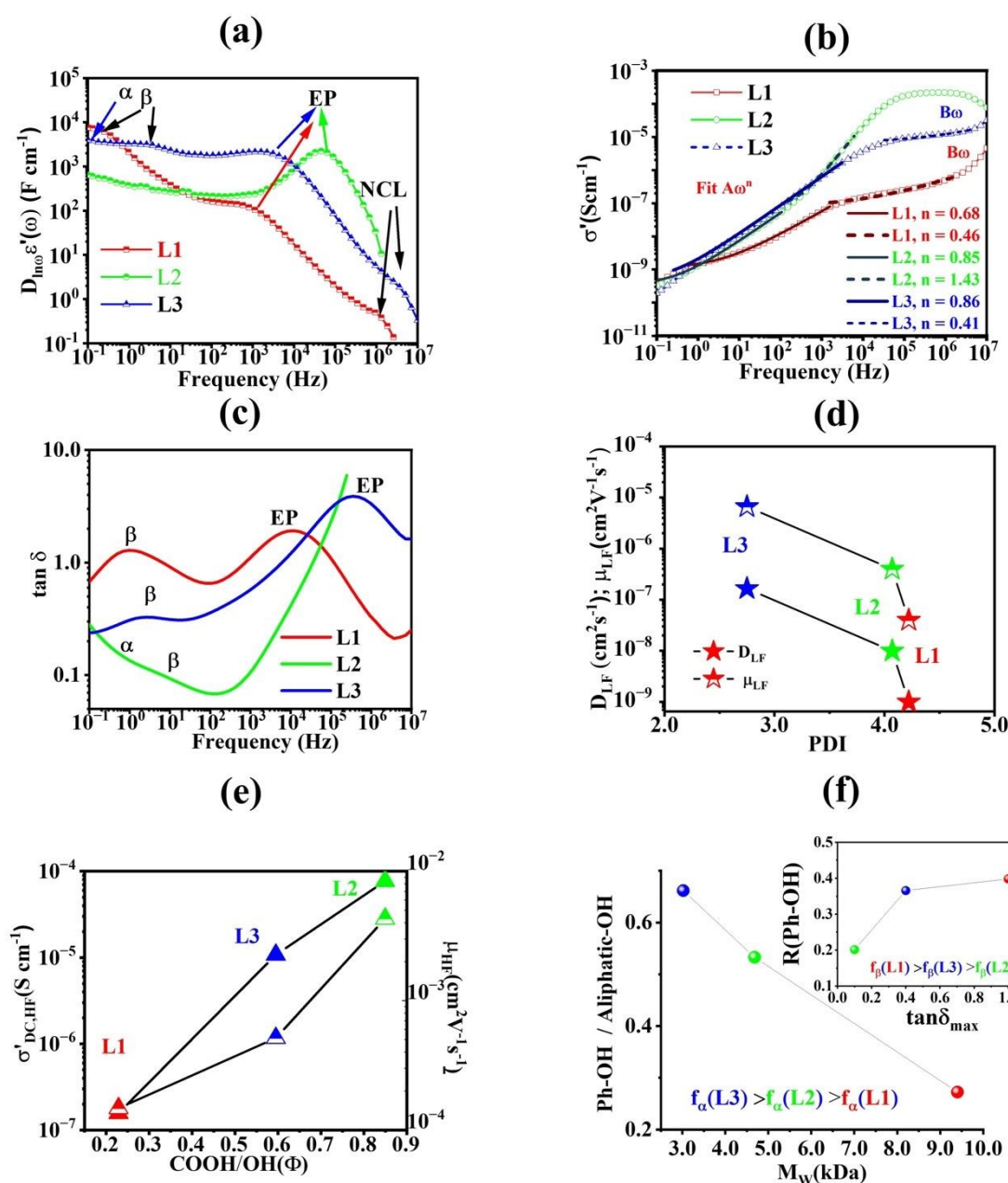


Figure 2. (a-c) Broadband dielectric spectroscopy results of lignins **L1**, **L2**, and **L3**. **(a)** Dielectric response $D_{ln\omega}\epsilon''(\omega)$ showing α , β , **EP** and **NCL** relaxations. **(b)** Real part of the AC conductivity (σ') fitted with Jonscher–Funke’s law $A\omega^n$ with $n < 1$ in **L1** and $n \geq 1$ in **L2** and **L3**. **(c)** Loss factor **tan δ** in log-log scale highlighting relaxation peaks. **(d-f)** Correlations between the BDS and chemical characterization parameters: **(d)** Conductivity σ_{HF} (left y-axis) and mobility μ_{HF} (right y-axis) vs. the COOH/OH ratio from the COOH and OH contents in **Table S1**. **(e)** low-frequency diffusion coefficient, D_{LF} , and charge mobility, μ_{LF} vs. PDI values in **Table S1**. **(f)** Correlation between the sequency in weight average (see **Table S1**) M_w (**Table S1**) in lignin and the ratio between the Phenyl -OH (Ph-OH) vs. Aliphatic-OH content, linked to the α -relaxation frequency shift; inset : correlation between the sequency of the ratio $R = \text{Ph-OH} / (\text{Ph-OH} + \text{Aliphatic-OH})$ and the magnitude of the peak in loss factor $\tan \delta$ related to β -relaxation in the label, the corresponding blue shift in the β -relaxation peak position of the frequency f_β (**Table S1** and **Figure 3c**)

The inspection of the AC conductivity enables to recognize two distinct regions in **L1**’s σ' plot (**red trace in panel 2b**), both following Jonscher–Funke’s law⁴⁸ (see **eq. S12** in the *BDS data analysis* section), where the power term, i.e., $A\omega^n$ with $n < 1$, has $n \sim 0.7$ at frequencies < 1.0 kHz and $n \sim 0.5$ at higher frequency. These correspond in $D_{ln\omega}\epsilon''(\omega)$ to the β -relaxation and the EP, respectively. The crossover region is linearly dependent on the frequency ($B\omega$, **eq. S10**), validating the NCL relaxation observed in $D_{ln\omega}\epsilon''(\omega)$ ⁴⁹. In **L2** (**panel 2b, green curve**), the behavior is noticeably distinct from the one of **L1**. **L2**’s previously reported n values¹³ prove that charge hopping occurs mainly through localized trap states ($A\omega^n$, $n \cong 1$, i.e., $n = 0.85$ up to 200 Hz and $n = 1.43$ up to 10 kHz)⁵⁰ and is followed by free ion charge diffusion, evidenced by a short curve plateau. **L3**’s conductivity behavior (**panel 2b, blue curve**) is intermediate between that of **L2** and **L1**: at low frequencies, it follows Funke’s law (with $n \approx 1$, specifically $n = 0.92$) as **L2**’s, whereas at high frequencies it conforms to Jonscher’s law ($n = 0.41$) and the Nearly Constant Loss (NCL) region as **L1**’s.

It is interesting the correlation of these findings with the three lignins morphologies. **Figure S1** shows the field emission scanning electron Microscopy (FE-SEM) micrographs of the three lignins. **L1** produced smooth, amorphous films with flat surfaces, reflecting its high solubility and lack of aggregate formation due to a high free phenol group content. In contrast, **L2** showed a rough surface with fibrous structures and agglomerates, which is attributed to its lower solubility. **L3** exhibited an intermediate morphology with some agglomerates and a rougher surface than **L1**, but better dispersion than **L2** due to its higher content of aliphatic hydroxyl groups, which facilitate hydrogen bonding with the solvent. It is noteworthy how the n values correlate strictly with the morphological structure, being $n < 1$ in **L1**, which displays a smoother homogenous surface like observed in amorphous materials, favoring delocalized ionic charge hopping transport mechanisms, and $n \geq 1$ in **L2**, which displays a more inhomogeneous structure, favoring more localized charge transport.⁵⁰ In **L3**, the presence of grains and grain boundaries explains the n value in the middle between those in



L1 and **L2**. Furthermore, the values of σ' at the plateau ($\sigma_{DC, HF}$) follow the sequence $\sigma_{DC, HF} (L1) (10^{-7} \text{ S cm}^{-1}) < \sigma_{DC, HF} (L3) (10^{-5} \text{ S cm}^{-1}) < \sigma_{DC, HF} (L2) (10^{-4} \text{ S cm}^{-1})$ in line with the R_{HF} one derived from NPs simulation and from the DC RT Current-Voltage measurements³⁰.

The loss factors $\tan \delta$ (**panel 2c**) connect the permittivity and conductivity results. In **L1** $\tan \delta$ (red curve in **Figure 2c**) features two well-resolved peaks, corresponding to the β -relaxation and EP, and confirming that the AC conductivity occurs through a superposition of two different ionic charge hopping mechanisms via delocalized states^{48,51}. Interestingly, in **L2**, the loss factor representation (green curve in **Figure 2c**) presents the tail of a peak at a frequency much lower than 0.1 Hz, which we referred to as the α -relaxation, accompanied by a small bump signaling the β -relaxation and a tail referred to the EP relaxation. In **L3**, the loss factor (blue curve in **Figure 2c**) exhibited a behavior more similar to **L1** than to **L2**, exhibiting only two visible peaks, corresponding to the β -relaxation and EP, with no evidence of the α -relaxation (**Figure 2a**). This aspect, with respect to the Kramers-Kronig representation, is justified by the DC conductivity contribution to loss factor, affecting the resolution of all the relaxation peaks, especially those at low frequency⁴¹. The conductivity $\sigma_{DC, HF}$ (**Figure 2e, left y-axis**) and mobility μ_{HF} (**2e, right y-axis**) values at the plateau correlate with the COOH (**Figure S6b,d**) and phenolic group $OH(\Phi)$ (**Figure S6a,c**) millimolar content of lignin. The values of $\sigma_{DC, HF}$ and μ_{HF} increase by approximately two orders of magnitude in the order **L1** < **L3** < **L2**. These parameters are plotted vs. the COOH/phenolic OH molar ratio (COOH/OH(Φ), **Figure 2d**) which grows in the same order. The two chemical functionalities exert a competitive effect on conductivity parameters: the COOH group provides H^+ protons as diffusive ionic charges, whilst the phenolic OH increases the pseudocapacitive behavior. Conversely, at low frequency, where localized hopping is the main transport mechanism, the D_{LF} , and the corresponding charge mobility, μ_{LF} (**Figure 2e**, and eq. S13 and S15) decrease in the order **L1** < **L2** < **L3**, and are found to be proportional to the polydispersity index (PDI) of the polymeric chains which decreases in the same order.

As a further result, we observe the frequency shift of the α -relaxation peak in the order **L1** < **L2** < **L3**. This correlates well with the lignin weight-average molecular weight, M_w (Table S1), in a sense that the lower the M_w the higher the frequency of the α -relaxation peak (**Figure 2f**). M_w is a measure of the average mass of molecules in a sample, giving more influence on larger molecules, and reflects their contribution to the α -relaxation mechanism. Finally, the mass weight M_w relates with the balance between the phenyl vs aliphatic-OH as seen in (**Figure 2f**). This is implicit as the highest is the extent of depolymerization, the highest number of phenolic groups are liberated, and depending on the extraction method, not all of them will be balanced by aliphatic alcohols, that can be subject to elimination processes.



The β -type relaxation is generally attributed to the hydration level, as previously reported by Ambrico et al.⁴³ In our study, all impedance measurements were performed under controlled laboratory conditions with a consistent relative humidity of approximately 50%. Therefore, the observed β -relaxation can be interpreted in the light of the hydrophilic or hydrophobic nature of the lignin samples. By analyzing the behavior of the loss factor, we observe that both the intensity and frequency position of the β -relaxation peak follow the sequence: **L1** > **L3** > **L2**. These findings suggest that a higher β -peak magnitude corresponds to a more hydrophilic character. Within this context, a strong correlation has been identified between β -relaxation and the relative content of aliphatic –OH groups. Additionally, this observation is consistent with the presence of aromatic condensation in the polymeric chains of **L2**, which contributes to its more hydrophobic nature and affects its ionic conductivity (see⁵² and references therein).

The chemical formula, specifically the sulfur/nitrogen (S/N) stoichiometric coefficient ratio, vs. the ash percentages in (**Table S1**, **Figure S7** of Supporting Information), suggests that **L1** and **L2** contain sulfates in their ashes as revealed by previous scanning electron microscopy - energy dispersive spectroscopy (SEM-EDS) analysis.^{7,53} The sulfated ashes have long been known to cause a linear increase in the electrical conductivity depending on their concentration.⁵³ Accordingly, the higher value of the plateau in the AC conductivity in **L2** can be explained as a combined effect of the ash content (25.3%), morphology and COOH/OH (Φ) ratio. In this framework, the ash may create conducting paths in **L2** aggregates allowing to reduce the energetic barrier to charge diffusion by the **L2** inhomogeneous morphology, also favoring a mixed ionic/electronic path. Conversely, in **L1**, the more uniform aggregate distribution favors the inter-aggregate delocalized hopping, whereas the much lower ash content and lower COOH/OH(Φ) ratio do not suggest an increase of the current due to free diffusion of ionic charges. Again, in **L3**, the conductivity falls between **L1** and **L3**. Considering the linear correlation of the ash content to the conductivity⁵³ and to the S/N ratio calculated from FWs (**Table S1**), we confirm this trend in plot **S7**, which is compatible with a rough estimation of ash at **L3** ~1.5%. Therefore, we can assume that the conductivity and capacitive properties of **L3** are essentially related to those of COOH/OH(Φ) ratio.

In summary, the BDS analysis revealed that, the dielectric relaxations of **L1**, **L2** and **L3** in the explored frequency range are closely related to the PDI (determining the mobility and diffusivity), to the hydration feature via the β -relaxation, and to the EP via the ion charge displacement. The lignin morphology is responsible for establishing *ionic charge hopping* (Jonscher–Funke’s law)^{50,51} with the COOH and OH (Φ) hydroxyl contents and their ratio regulating the carrier transport mechanisms, mainly free ion charge diffusion and displacement. The former, being under conditions approaching



the DC I–V conditions, displayed conductivity values in line with those observed in the IV characteristics under a DC electric field. Moreover, a peculiar role is believed to be played by the ash content in determining mixed electronic/ionic conduction in **L2**. Within our samples set, ash content modulates both the AC conductivity plateau and the capacitive window. **L2** (25.3% ash) shows a doping-like enhancement of mixed ionic/electronic pathways, a low HF resistive intercept, and a Gerischer element under ± 0.8 V, consistent with sulfate-rich ashes. Conversely, **L1** (~3.1% ash) and **L3** (ash negligible, ~1.5% estimated from S/N) fall in a low-ash regime where dielectric/capacitive properties are governed primarily by COOH/OH chemistry and morphology. Operationally, our data indicate minimal impurity impact for $\lesssim 3\%$ ash and a marked effect in a high-ash regime ($\gtrsim 20\%$).

2.3 Supercapacitive properties of lignins: applications

The supercapacitor (SC) performance of lignin-based devices (**L1**, **L2**, and **L3**) is evaluated through the power representation of their impedances, specifically by analyzing the complex power³⁵

$$S(\omega) = P_{Act}(\omega) - jQ_{React}(\omega).$$

of the reactive power, $Q_{React}(\omega)$ and active power, $P_{act}(\omega)$, calculated via the real C_p' and imaginary C_p'' parts of the capacitance and represented in **Figures 3b-d** as the values normalized to the module of the power S , $|S|$ (compare ESI, equations **S16-S20**).

In lignin **L1** (Figure 4b), $P_{Act}(\omega)$ and $Q_{React}(\omega)$ do not present clear transition point from capacitive to resistive states, and multiple relaxation phenomena are driven mainly by two superimposed hopping mechanisms, limiting the development of net charge displacement and then the onset of more capacitive behavior. These behaviors reflect the structural complexity, disordered nature of **L1** and moderate ash content (3.1%), and low ionic charge mobility and summarizes confinement, which hinder supercapacitor performance. (**Figure 3b**)



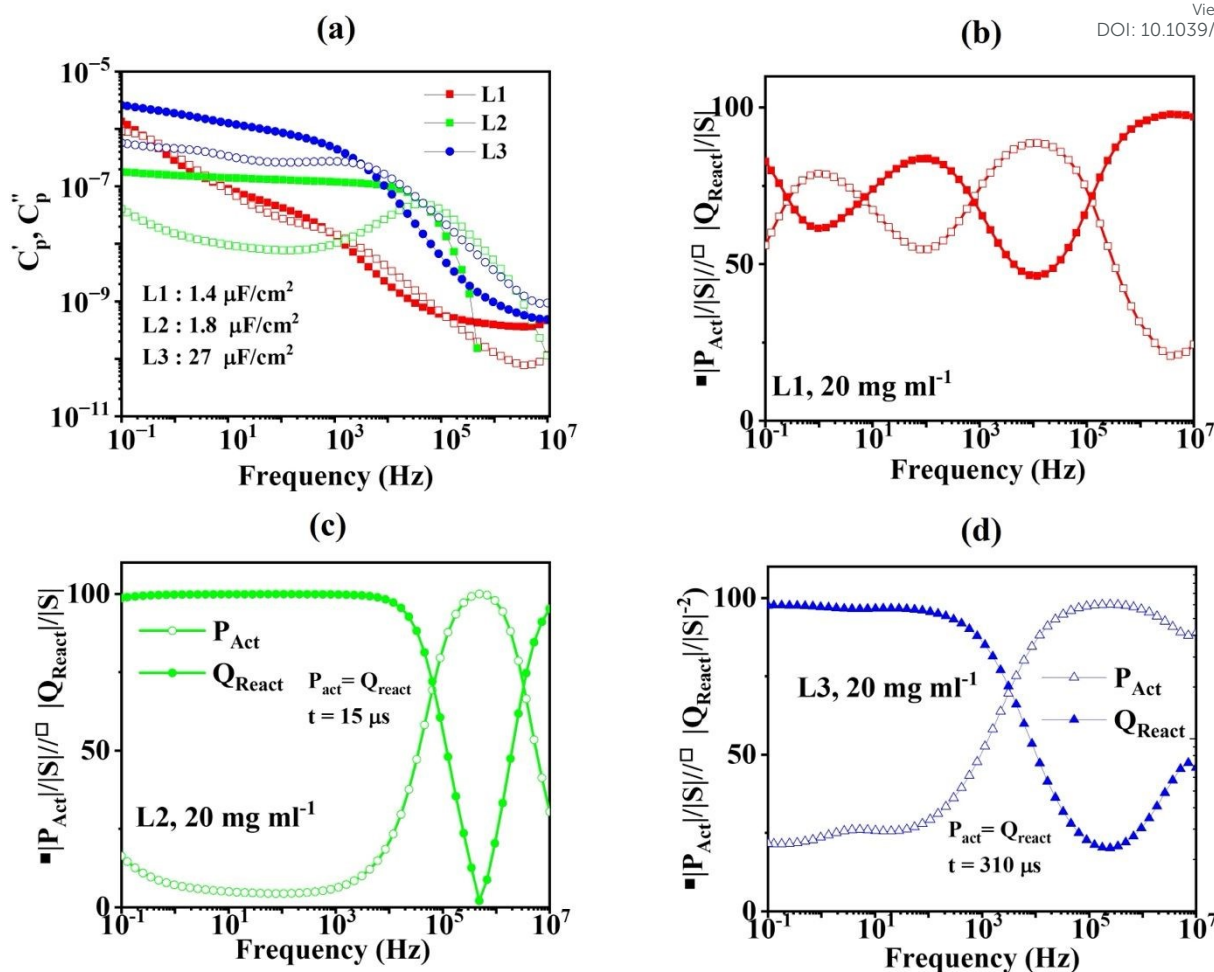


Figure 3. (a) Values of the real C_p' (solid squares) and imaginary C_p'' (hollow squares) part vs. f of the capacitance as calculated from impedance data (expr.S16-S17) In the label the values of the C_{areal} (Table 1) at 0.1 mHz are reported. (b) Reactive power (Q_{React} , solid symbols) and active power (P_{act} , hollow symbols) normalized to the module of the complex power $S = Q_{\text{React}} + j P_{\text{act}}$ as a function of frequency for (b) L1, (c) L2, and (d) L3; in L2 and L3 the crossover frequency between (Q_{React}) and (P_{act}) (i.e. $Q_{\text{React}} = P_{\text{act}}$) were 67 kHz and 3.2 kHz respectively corresponding to $t = 15 \mu\text{s}$ and $t = 310 \mu\text{s}$ The volumetric capacitance, energy and power densities are summarized in Table 1.⁵⁴



Table 1. Areal and Volumetric capacitance, energy and power densities estimated at 0.1 Hz for the three lignins and $Q_{\text{react}}/P_{\text{act}}$ crossover frequencies.

ITEM	$C_{\text{areal}}^{\text{s}}$ ($\mu\text{F cm}^{-2}$)*	C_{Vo}^{s} (F cm^{-3})*	$E_{\text{d,vol}}$ (mW cm^{-3})*	$E_{\text{d,areal}}$ (mW cm^{-2})*	$P_{\text{d,vol}}$ (mW cm^{-3})*	$P_{\text{d,areal}}$ (mW cm^{-2})
L1	14	2.15			-	
L2	1.8	0.28	8.0	5.0	2.0	0.16
L3	27	4.13	117	10	26	2.0

* V_{strip} = Estimated single cell volume referred to the strip between each couple of fingers infiltrated by the lignin: $V_{\text{strip}} = \phi \times w \times l = 0.35 \text{ cm} \times 10 \mu\text{m} \times 200 \text{ nm}$; $V_{\text{tot}} = 90 \times V_{\text{strip}}$ estimated only for lignin displaying SC behavior^s; Σ = lignin layer section crossed by the electric field lines: $\Sigma = \phi \times l = 0.35 \times 200 \times 10^{-7}$; value of the lignin layer section crossed by the electric field lines taken for the estimate of the areal parameters. $C_{\text{vol}} = C_p' (0.1 \text{ Hz}) / V_{\text{tot}}$; $C_{\text{areal}} = C_p' (0.1 \text{ Hz}) / \Sigma$; $E_{\text{d,vol}} = Q_{\text{react}} (0.1 \text{ Hz}) / V_{\text{tot}}$; $E_{\text{d,areal}} = Q_{\text{react}} (0.1 \text{ Hz}) / \Sigma$; $P_{\text{d,vol}} = P_{\text{act}} (0.1 \text{ Hz}) / V_{\text{tot}}$; $P_{\text{d,areal}} = P_{\text{act}} (0.1 \text{ Hz}) / \Sigma$; ϕ : diameter of the IDE cell; w = finger gap; l = Ti/Au contact thickness; (see also ESI and representative sketch in **Figure S8**)

Moreover, considering the results in **Figure 3d** and **Figure S6**, the relatively high content of phenolic hydroxyls ($\text{OH}(\Phi) = 1.31 \text{ mmol/g}$ of lignin) suggests a strong pseudocapacitive contribution that, together with the limited density of carboxyl groups ($\text{COOH} = 0.30 \text{ mmol/g}$ of lignin), inhibits ionic diffusion, contributing to the oscillatory behavior observed in P_{Act} and Q_{React} and its reduced SC performance. On the other hand, **L2** in panel c) exhibited a sharp capacitive-to-resistive transition at a frequency of 67 kHz and estimated at the crossover when $P_{\text{act}} = Q_{\text{react}}$ and corresponding to a rise time ($t = 15 \mu\text{s}$). (**Figure 3c**)

At low frequencies, Q_{React} dominates, indicating efficient charge storage. The rapid transition at higher frequencies to $P_{\text{Act}}(\omega) > Q_{\text{React}}(\omega)$, i.e., from a capacitive to a low resistive behavior mimicking the DC current response, reflects excellent mixed ionic and electronic conductivity, which is further attributed to the higher ash content. Furthermore, the wide frequency range showing capacitive behavior together with the rapid transition indicate interesting SC properties. The SC performance of **L2** can be further explained as a combined effect due to its high ash content (25.3%). Furthermore, while fibrous morphologies are often advantageous for charge transport, SEM analysis of **L2** suggests a less uniform distribution of fibrous domains. This heterogeneity may introduce energy barriers to ion hopping at low frequencies, where ions must move across distant aggregates or grain boundaries. However, the high ash content (25.3%) increases electronic conductivity, particularly at high frequencies, probably through a doping-like effect. Consequently, the synergy between fibrous morphology, hydroxyl functionality and ash content favors efficient charge transport over a wide frequency range. The balance between the phenolic hydroxyl content ($\text{OH}(\Phi) = 0.73 \text{ mmol/g}$ of lignin) and the high carboxylic group density ($\text{COOH} = 0.62 \text{ mmol/g}$ of lignin) equilibrates



the capacitance and ionic conductivity and supports its rapid capacitive–resistive transition and overall SC performance. The frequency of the resistive vs. capacitance transition at **L3** occurs at approximately 1.0 kHz, (panel d) estimated at $f = 3.7$ kHz corresponding to the crossover frequency when $Q_{\text{react}} = P_{\text{react}}$ at $f = 3.7$ kHz and $t = 312$ μs , (**Figure 3d**) which is one order of magnitude slower than that at **L2**. Like **L2**, **L3** demonstrated strong capacitive behavior at low frequencies, with dominating Q_{React} . The highest aliphatic hydroxyl content ($\text{OH} = 2.90$ mmol/g of lignin) enhances hydration, supporting **L3**'s capacitive behavior at low frequencies. Moreover, the moderate phenolic hydroxyl content ($\text{OH}(\Phi) = 0.79$ mmol/g) and intermediate carboxylic group density ($\text{COOH} = 0.47$ mmol/g) provide a balance between the pseudocapacitive and ionic contributions. These chemical features, combined with potential structural inhomogeneities and internal defects and an undetectable ash content, likely contribute to the slower capacitive-to-resistive transition than that of **L2**. Despite the slower transition dynamics, **L3** retains a significant SC potential because of its capacitive behavior at low frequencies and the combined effects of its hydroxyl functionalities and molecular structures. In summary, the SC performances of the three lignins **L1**, **L2** and **L3** are a consequence of the combination of chemical and morphological features, both of which contribute to tuning the onset or absence of a transition from capacitive to resistive behavior.

Operationally, **L2** sustains capacitive fast operation with the lowest HF resistance intercept, while **L3** combines robust LF capacitance with cleaner chemistry, two distinct, application-relevant profiles. Notably, the areal and volumetric capacitance values - consistent with recent benchmarks - combined with an extended frequency range and energy conversion efficiency surpassing 95%, establish a strong and promising foundation for future sustainable, high-speed lignin-based microsupercapacitor device engineering. However, targeted efforts to enhance energy and power densities remain essential to fully unlock their potential.

3. Conclusions

This study analyzed three different lignins (**L1**, **L2**, and **L3**) in response to an alternating electric field using Nyquist Plots, Broadband Dielectric Spectroscopy, and Complex Power. A correlation was found between the chemical, structural, and morphological properties and the electrical parameters such as AC conductivity, diffusivity, and mobility. Our analysis uses a consistent modeling framework for all lignins (shared BDS formalism and base EIS circuit), with a parsimony rule that adds a single LF diffusion/chemical term only when the data require it (e.g., the Gerischer feature under bias in **L2/L3**). As a result, the comparison is done on model-robust metrics extrapolated



directly from the data - the HF resistive intercept, the extent of capacitive dominance and its transition frequency, and BDS-derived mobility/diffusivity - rather than on fit-sensitive parameters. This makes the observed differences attributable to intrinsic material physics, not methodological choices. The results show that **L2** and **L3**, especially at 0.0 V DC, exhibit behavior similar to materials used in supercapacitors. **L1** shows a mixed behavior at both high and low frequencies, while **L2**, with its fibrous morphology, quickly transitions to an ideal capacitive state. **L3**, on the other hand, shows an intermediate behavior, similar to **L1** at high frequencies but dominated by capacitive effects at low frequencies. At 0.8 V, **L2** and **L3** show increased interaction with the external environment, supported by the presence of a Gerisher-type impedance, suggesting greater reactivity toward atmospheric gases. The reactivity of lignin appears to be linked to the OH content, particularly the aliphatic -OH groups. The BDS representations show how polymer structure influences reactivity and charge mobility, with **L3** exhibiting lower polymerization than **L1** and **L2**. AC conductivity varies based on morphology: **L1** exhibits delocalized ionic charge transport, while **L2** shows more localized transport. Impurities matter chiefly in high-ash lignins: **L2** (25.3%) exemplifies a regime where ashes promote mixed conduction and accelerate the capacitive-to-resistive transition, whereas in low-ash or ash-free materials ($\approx 0\text{--}3\%$) the dielectric and supercapacitive responses are dictated by hydroxyl/carboxyl chemistry and morphology. **L3** demonstrates a good balance of chemical and morphological properties, favoring strong ionic transport and capacitive performance. The comparative analysis presented herein on **L1**, **L2** and **L3** underscores that lignin performance is strongly influenced by its origin and extraction method. Commercial Kraft lignins provide industrially relevant benchmarks, while the *organosolv* **L3** offers higher purity and higher structural homogeneity. Selecting lignins with such contrasting structural and chemical characteristics enables evaluation across both abundant industrial feedstock's and high-value reactive lignin, guiding the design of sustainable, next-generation electronic materials. The analysis of SC-related parameters in **L2** and **L3** together with the device configuration adopted evidence that **L2** and **L3** exhibit complementary capacitive strengths and chemistry, aligning with benchmark capacitance values and high energy efficiency, offering a strong basis for future lignin-based microsupercapacitor development. The response similar to that of supercapacitors of **L2** and the chemically cleaner profile of **L3**, together with the higher estimated values of the volumetric capacitance/energy/power, are directly reflected in two application paths: ready-to-use charge storage and purity-oriented dielectric-capacitive layers, respectively. The EIS fingerprints used here translate into practical acceptance criteria for large-scale coated devices. Therefore, our findings translate into actionable quality assurance (QA) anchors, including incoming C_0 calibration and EIS-derived fingerprints used as pass/fail criteria within a defined operating window (± 0.8 V). The established correlations between chemical composition and electrochemical

View Article Online
DOI: 10.1039/D5TA05024C



performance enable the formulation of procurement specifications and batch ranking. Among the tested materials, *organosolv* lignin emerges as the most application-ready, while selected technical lignins also qualify, provided they meet defined thresholds for impurity levels and electrical performance.

Author contributions

M.A. Conceptualization, Methodology, Investigation, Formal analysis, Supervision, Writing - Original Draft, Writing – Review & Editing, Funding Acquisition.

O.D. Investigation, Formal Analysis, Supervision, Writing - Original Draft, Writing – Review & Editing.

S.D.S. Investigation, Data Curation, Writing – Review & Editing.

R.D. Investigation, Data Curation, Writing – Review & Editing.

D.A. Investigation, Data Curation, Writing – Review & Editing.

P.F.A. Formal Analysis, Writing – Review & Editing, Funding Acquisition.

N.M. Investigation, Formal Analysis, Writing – Review & Editing.

F.G. Investigation, Formal Analysis, Writing – Review & Editing.

S.R. Investigation, Formal Analysis, Writing – Review & Editing, Funding Acquisition.

A.O. Investigation, Supervision, Formal Analysis, Writing - Original Draft, Writing – Review & Editing, Funding Acquisition.

A.D.B. Supervision, Formal Analysis, Writing – Review & Editing, Funding Acquisition.

Conflicts of interest

There are no conflicts to declare.

Data Availability

The data supporting the findings of this study are available within the article and its Supplementary Information files. Detailed experimental procedures, characterization data (including elemental analysis, GPC, and ³¹P-NMR spectroscopy), and electrical measurements (EIS, BDS, and Nyquist plots) are provided in the Supplementary Information document. Additional raw data and analysis files are available from the corresponding authors upon reasonable request.



Acknowledgments

View Article Online
DOI: 10.1039/D5TA05024C

The authors are grateful to Prof. Anna Maria Raspolli Galletti and Prof. Franco Cotana for providing the steam exploded cardoon. FE–SEM micrographs were acquired at the Center for Instrument Sharing of the University of Pisa (CISUP). A.D.B. and O.D. acknowledge the financial support from the University of Salerno, with grants ORSA223384 and ORSA235199. R.D. and A.O. acknowledge the University of Pisa for funding “BIHO 2022 – Bando Incentivi di Ateneo Horizon e Oltre” (Prot. n. 0048740/2022). S.R. acknowledges the funding of MCIN/AEI/10.13039/501100011033 and EU NextGeneration EU/PRTR (RYC2021-031964-I). S.R. and A.O. acknowledge Consellería de Cultura, Educación, Formación Profesional y Universidades (Xunta de Galicia) (ED431F2023/03). M.A. and P.F.A. acknowledge the Italian Ministry of University and Research (MUR) PONa3_00369 SISTEMA. For P.F.A and D.A.: this work was supported by Regione Puglia, Riparti - POC PUGLIA FESRT-FSE 2014/2020. D.A. thanks Italian National Recovery and Resilience Plan (NRRP), funded by the European Union—NextGenerationEU (Mission 4, Component 2, Investment 3.1—Area ESFRI Energy—Call for tender No. 3264 of 28-12-2021 of Italian University and Research Ministry (MUR), Project IDIR0000007 ‘NEFERTARI—’, MUR Concession Decree No.243 del 04/08/2022, CUP B53C22003070006). Views and opinions expressed are however those of the author(s) only and do not necessarily reflect those of the European Union or the European Commission. Neither the European Union nor the European Commission can be held responsible for them.

References

- 1 Y. Park and J.-S. Lee, *ACS Appl. Mater. Interfaces*, 2017, **9**, 6207–6212.
- 2 V. K. Thakur, M. K. Thakur, P. Raghavan and M. R. Kessler, *ACS Sustainable Chem. Eng.*, 2014, **2**, 1072–1092.
- 3 T. Y. Nilsson, M. Wagner and O. Inganäs, *ChemSusChem*, 2015, **8**, 4081–4085.
- 4 C. Lai, Z. Zhou, L. Zhang, X. Wang, Q. Zhou, Y. Zhao, Y. Wang, X.-F. Wu, Z. Zhu and H. Fong, *Journal of Power Sources*, 2014, **247**, 134–141.
- 5 Y. She, X. Li, Y. Zheng, D. Chen, X. Rui, X. Lin and Y. Qin, *Energy & Environ Materials*, 2024, **7**, e12538.
- 6 S. Kim, Y. K. Kim, H. Lee, S. B. Lee and H. S. Park, *ChemSusChem*, 2014, **7**, 1094–1101.
- 7 R. D’Orsi, C. V. Irimia, J. J. Lucejko, B. Kahraman, Y. Kanbur, C. Yumusak, M. Bednorz, F. Babudri, M. Irimia-Vladu and A. Operamolla, *Advanced Sustainable Systems*, 2022, **6**, 2200285.
- 8 J. Zhu, C. Yan, X. Zhang, C. Yang, M. Jiang and X. Zhang, *Progress in Energy and Combustion Science*, 2020, **76**, 100788.
- 9 W. E. Tenhaeff, O. Rios, K. More and M. A. McGuire, *Adv Funct Materials*, 2014, **24**, 86–94.
- 10 W. Zhang, J. Yin, Z. Lin, H. Lin, H. Lu, Y. Wang and W. Huang, *Electrochimica Acta*, 2015, **176**, 1136–1142.
- 11 S. S. Khviyuzov and A. S. Volkov, *Polymers for Advanced Techs*, 2024, **35**, e6467.
- 12 S. Khviyuzov, K. Bogolitsyn, A. Volkov, G. Kuposov and M. Gusakova, *Holzforchung*, 2020, **74**, 1113–1122.
- 13 S. De Stefano, O. Durante, R. D’Orsi, A. Operamolla, M. Ambrico, P. F. Ambrico, N. Martucciello, F. Giubileo and A. Di Bartolomeo, *J. Mater. Chem. C*, 2024, **12**, 13621–13631.



- 14 M. Khalid Rahmani, S. Ali Khan, M. Farooq Khan and M. Hee Kang, *Materials Science and Engineering: B*, 2022, **282**, 115784.
- 15 R. D'Orsi, J. J. Lucejko, F. Babudri and A. Operamolla, *ACS Omega*, 2022, **7**, 25253–25264.
- 16 D. S. Bajwa, G. Pourhashem, A. H. Ullah and S. G. Bajwa, *Industrial Crops and Products*, 2019, **139**, 111526.
- 17 S. Sethupathy, G. Murillo Morales, L. Gao, H. Wang, B. Yang, J. Jiang, J. Sun and D. Zhu, *Bioresource Technology*, 2022, **347**, 126696.
- 18 A. Sakakibara, *Wood Sci. Technol.*, 1980, **14**, 89–100.
- 19 H. Erdtman, *J. Polym. Sci. B Polym. Lett.*, 1972, **10**, 228–230.
- 20 C. J. Biermann, *Handbook of pulping and papermaking*, Elsevier, 1996.
- 21 S. Sharma, A. Sharma, S. I. Mulla, D. Pant, T. Sharma and A. Kumar, in *Lignin*, eds. S. Sharma and A. Kumar, Springer International Publishing, Cham, 2020, pp. 1–15.
- 22 D. Kai, M. J. Tan, P. L. Chee, Y. K. Chua, Y. L. Yap and X. J. Loh, *Green Chem.*, 2016, **18**, 1175–1200.
- 23 R. D'Orsi, N. Di Fidio, C. Antonetti, A. M. Raspolli Galletti and A. Operamolla, *ACS Sustainable Chem. Eng.*, 2023, **11**, 1875–1887.
- 24 B. R. Matos, R. Politano, J. F. Q. Rey, D. Hermida-Merino, U. Schade, L. Puskar and F. C. Fonseca, *Scientific Reports*, 2018, **8**, 13441.
- 25 M. Ambrico, L. Guazzelli, A. Mezzetta, A. Cariola, L. Valgimigli, P. F. Ambrico and P. Manini, *Journal of Molecular Liquids*, 2024, **403**, 124892.
- 26 P. Frübing, F. Wang, T. F. Kühle and R. Gerhard, *Applied Physics A: Materials Science and Processing*, 2016, **122**, 1–10.
- 27 A. A. Khamzin, I. I. Popov and R. R. Nigmatullin, *Physical Review E - Statistical, Nonlinear, and Soft Matter Physics*, DOI:10.1103/PhysRevE.89.032303.
- 28 J. E. B. Randles, *Discuss. Faraday Soc.*, 1947, **1**, 11.
- 29 K. A. Motovilov, V. Grinenko, M. Savinov, Z. V. Gagkaeva, L. S. Kadyrov, A. A. Pronin, Z. V. Bedran, E. S. Zhukova, A. B. Mostert and B. P. Gorshunov, *RSC Advances*, 2019, **9**, 3857–3867.
- 30 R. D'Orsi, S. De Stefano, O. Durante, M. Ambrico, D. Aceto, F. Ambrico, N. Martucciello, F. Giubileo, S. Rivas, A. Amperomolla and A. D. B. Bartolomeo, *JPhys Materials*, 2025, **8**, 045003.
- 31 E. Barsoukov and J. R. Macdonald, Eds., *Impedance Spectroscopy: Theory, Experiment, and Applications*, Wiley, 1st edn., 2005.
- 32 A. L. Pomerantsev, *Progress in chemometrics research*, Nova Publishers., 2005.
- 33 B. Boukamp, *Solid State Ionics*, 2003, **157**, 29–33.
- 34 P. Johnson, *Journal of Chemometrics*, 2005, **19**, 266–267.
- 35 P. L. Taberna, P. Simon and J. F. Fauvarque, *J. Electrochem. Soc.*, 2003, **150**, A292.
- 36 R. G. A. P. A. L. Bondarenko A. S., In *Progress in Chemometrics Research Ed.*; Nova Science Publishers: New York, <http://www.abc.chemistry.bsu.by/vi/analyser/>.
- 37 P. Johnson, *Journal of Chemometrics*, 2005, **19**, 266–267.
- 38 A. J. Bard and L. R. Faulkner, *Electrochemical methods: fundamentals and applications*, Wiley, New York Weinheim, 2. edition., 2001.
- 39 A. S. Merenga, C. M. Papadakis, F. Kremer, J. Liu and A. F. Yee, *Colloid Polym Sci.*, 2001, **279**, 1064–1072.
- 40 F. Fanari, C. Iacob, G. Carboni, F. Desogus, M. Grosso and M. Wilhelm, *LWT*, DOI:10.1016/j.lwt.2022.113345.
- 41 M. Nakanishi and A. P. Sokolov, *Journal of Non-Crystalline Solids*, 2015, **407**, 478–485.
- 42 B. Natesan, N. K. Karan and R. S. Katiyar, *Phys. Rev. E*, 2006, **74**, 042801.
- 43 M. Ambrico, A. B. Mostert, P. F. Ambrico, J. Phua, S. Mattiello and R. Gunnella, *Journal of Physics D: Applied Physics*, 2024, **57**, 265303.
- 44 M. Wübbenhorst and J. Van Turnhout, *Journal of Non-Crystalline Solids*, 2002, **305**, 40–49.
- 45 B. R. Matos, R. Politano, J. F. Q. Rey, D. Hermida-Merino, U. Schade, L. Puskar and F. C. Fonseca, *Sci Rep*, 2018, **8**, 13441.
- 46 Trukhan, E. M., *Soviet Physics-Solid State*, 1963, **4(12)**, 2560–2570.
- 47 J. Yuval and S. A. Safran, *Phys. Rev. E*, 2013, **87**, 042703.
- 48 A. K. Jonscher, *Nature*, 1977, **267**, 673–679.
- 49 T. S. Sørensen and V. Compañ, *J. Chem. Soc., Faraday Trans.*, 1995, **91**, 4235–4250.
- 50 K. Funke, *Progress in Solid State Chemistry*, 1993, **22**, 111–195.
- 51 A. K. Jonscher, *J. Phys. D: Appl. Phys.*, 1999, **32**, R57–R70.



52 A. Lisý, A. Ház, R. Nadányi, M. Jablonský and I. Šurina, *Energies*, 2022, **15**, 6213.

53 F. W. Zerban and Louis. Sattler, *Ind. Eng. Chem. Anal. Ed.*, 1931, **3**, 41–43.

54 M. J. Kim, M. Kim, W. B. Sohn, J. Kang, W. Kim and J. G. Kang, *Advanced Energy Materials*, 2024, **14**, 2402322.

View Article Online
DOI: 10.1039/D5TA05024C



Data Availability Statement

View Article Online
DOI: 10.1039/D5TA05024C

Lignin for sustainable electronics: Interplay of structure, morphology and chemistry in modelling dielectric properties

Marianna Ambrico, Ofelia Durante, Sebastiano De Stefano, Rosarita D'Orsi, Domenico Aceto, Paolo Francesco Ambrico, Nadia Martucciello, Filippo Giubileo, Sandra Rivas, Alessandra Operamolla, and Antonio Di Bartolomeo

***Corresponding authors:** odurante@unisa.it, alessandra.operamolla@unipi.it

The data supporting the findings of this study are available within the article and its Supplementary Information files. Detailed experimental procedures, characterization data (including elemental analysis, GPC, and ^{31}P -NMR spectroscopy), and electrical measurements (EIS, BDS, and Nyquist plots) are provided in the Supplementary Information document. Additional raw data and analysis files are available from the corresponding authors upon reasonable request.

